Available online at www.sciencedirect.com

ScienceDirect

Ceramics International 40 (2014) 257–262

CERAMICS INTERNATIONAL

www.elsevier.com/locate/ceramint

On the possibility of hercynite formation in a solid state reaction at the Al_2O_3–iron interface: A density-functional theory study

Lilit Amirkhanyan[a], Torsten Weissbach[a,*], Jens Kortus[a], Christos G. Aneziris[b]

[a]Institute of Theoretical Physics, TU Bergakademie Freiberg, Leipziger Str. 23, D-09596 Freiberg, Germany
[b]TU Bergakademie Freiberg, Institut für Keramik, Glas- und Baustofftechnik, Agricolastraß 17, D-09596 Freiberg, Germany

Received 22 February 2013; received in revised form 21 May 2013; accepted 22 May 2013
Available online 7 June 2013

Abstract

Based on ab initio density functional theory calculations we discuss the possibility of hercynite formation at the interface of a ceramic Al_2O_3 based filter and a metallic melt. In particular a direct reaction is not favored, but an indirect path with the formation of hercynite through reactive FeO is more likely.

Keywords: B. Interfaces; D. Al_2O_3; D. Spinels; Density Functional Theory calculations

1. Introduction

High quality materials with well controlled properties build the basis of any modern technological application. Not surprising there is increasing demand from metal making and metal using industry to remove solid and liquid inclusions to improve the metal purity. The inclusions are formed for instance by deoxidation products, sulfides, nitrides or carbides [1]. In view of mechanical properties it is well known that size, type and distribution of such non-metallic inclusions in metal cast products are highly relevant for failure behavior. Therefore, one way to better materials is filtration of the metallic melt to remove endogenous as well as exogenous inclusions. Interestingly, inclusions in the several ten micrometer range can be filtered effectively using ceramic filters using pores in the millimeter range [2]. A similar process known from continuous steel casting, called clogging, happens when particles in the melt deposit as layers on the walls of a nozzle [3].

Studies on ceramic filters after use have registered that oxide and also iron particles stick to the surface, and in particular the formation of spinel $FeAl_2O_4$ (hercynite) [2]. To achieve a high filtration efficiency, the particles from the melt need to be rather strongly attached to the filter surface which is often provided by sintering processes. A reaction producing hercynite from iron and alumina was observed in arc-melting experiments [4].

In this paper, we study selected solid state reactions of corundum (Al_2O_3) with iron which may occur at a ceramic filter and metallic melt interface by means of density-functional theory (DFT). DFT presents an approximate solution to the quantum mechanical Schrödinger equation and allows for the calculation of ground state energies and geometries without the need for experimental input. We calculate the enthalpy as a function of pressure for several compounds in the system Al–O–Fe, which allows then to discuss chemical reactions in terms of enthalpy differences between starting and resulting compounds. Section 2 will introduce the crystal structures of the selected systems under consideration and the model parameters used. The computational details are reported in Section 3 and the results are discussed in Section 4. Section 5 contains our conclusions.

2. Crystal structures

2.1. Al_2O_3

For alumina, we studied three of the known polytype crystal structures. The thermodynamical stable structure under normal conditions is corundum ($\alpha-Al_2O_3$) with rhombohedral space

*Corresponding author. Tel.: +49 3731394034; fax: +49 3731394005.
E-mail address: torsten.weissbach@physik.tu-freiberg.de (T. Weissbach).

0272-8842/$ - see front matter © 2013 Elsevier Ltd and Techna Group S.r.l. All rights reserved.
http://dx.doi.org/10.1016/j.ceramint.2013.05.132

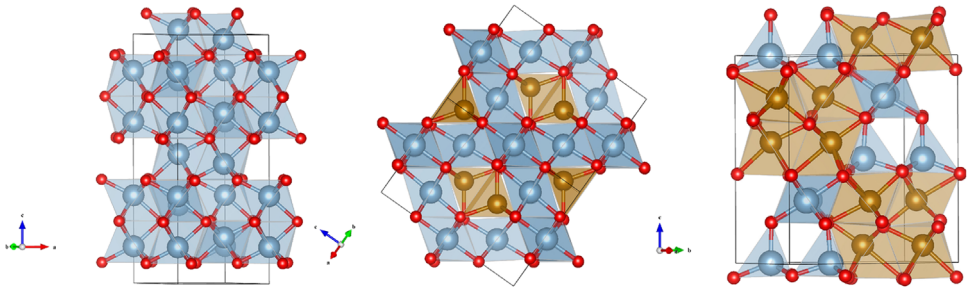

Fig. 1. Three of the discussed alumina and Fe–alumina structure types, with the layered structure and coordination polyhedra emphasized. Left: corundum, middle: spinel ($FeAl_2O_4$), and right: $AlFeO_3$. The balls redundant in blue color represent Al atoms, Fe and O are orange and red, respectively. (For interpretation of the references to color in this figure legend, the reader is referred to the web version of this article.)

group symmetry $R\overline{3}c$. An image of this structure is presented on the left panel of Fig. 1.

Depending on the method of preparation also other, metastable structures can form. One of them is $\kappa-Al_2O_3$, an orthorhombic ($Pna2_1$) [5] non-centrosymmetric structure. It belongs to the structure type of $FeAlO_3$ and thus could be a good candidate for Fe substitution.

The third structure is the $\gamma-Al_2O_3$ modification, a defect-spinel structure with aluminum vacancies. For a model of the $\gamma-$phase, it is therefore important to know the location of the vacancies. A previous DFT study [6] concludes that the lowest energy structure contains vacancies at octahedral sites. We will use that structural model in the present work.

All these structures can be described by layers of Al–O polyhedra with different stacking sequences. The stable corundum contains only Al–O octahedra, whereas γ and κ also exhibit tetrahedra. The links between different polyhedra also characterize the different crystal structures. In corundum, polyhedra share corners and full faces (i.e. 3 common atoms). The two metastable phases contain shared corners and shared edges (2 atoms) only.

2.2. FeO

This is a ferrous oxide with mineral name wuestite containing Fe^{2+} ions. It is usually formed only under reducing conditions, otherwise iron oxides form as Fe_2O_3 (hematite) and Fe_3O_4 (magnetite) compounds. Its composition under normal conditions is not stoichiometric, owing to the formation of Fe^{3+} [7]. In steel casting, it is frequently found [1] because of the low oxygen concentrations involved here. The crystal structure is of an fcc rock-salt type and the low-temperature phase is reported as antiferromagnetic [7]. We allowed for antiferromagnetism through lowering of the crystal symmetry of the unit cell in our fully stoichiometric model calculations.

2.3. Al–Fe oxides

The spinel $FeAl_2O_4$, with mineral name hercynite, can be formed during the filtering process [2] and is observed as one of the phases responsible for clogging of the filters. The chemical composition indicates Fe in oxidation state +2, where Fe prefers tetrahedral, and Al octahedral sites of the spinel. The structure is displayed in the middle of Fig. 1. Only a small degree of site disorder is expected [8]. Our model has ideally ordered sites and ferromagnetic ordering of the iron atomic moments. In addition, the site-exchanged Fe_2AlO_4 is considered here. In a DFT study [9], this compound is proposed having an inverse spinel structure. In this case, Fe occupies both tetrahedral and octahedral sites of the spinel structure, while Al is found only on the octahedral sites. Consequently, Fe occurs in both oxidation states +2 and +3. Although at present, we found no experimental observation of this structure, it can be considered as an extreme example for site disordered hercynite. In our calculations this inverse spinel is a metal with different magnetic moments on the two Fe sites. Due to the antiferromagnetic ordering and site dependent atomic magnetic moments, the compound is a ferrimagnet. Both oxides are metallic conductors.

As a second mixed oxide, we consider $FeAlO_3$. This is a complex material, crystallizing in the same orthorhombic structure as $\kappa-Al_2O_3$. It exhibits ferrimagnetism [10] and complex multiferroic behavior [11]. Regarding the ionic charges, Fe is in oxidation state +3 here. Unlike $FeAl_2O_4$, Fe prefers an octahedral coordination in this compound, while the Al sites have either octahedral or tetrahedral environment (see right panel of Fig. 1). The ferrimagnetism is approximated by an antiferromagnetic ordering in our model. The formation of $FeAlO_3$ in the solid state is unlikely, because its melting temperature is below than that of iron.

2.4. Metals

If Al_2O_3 decomposes, it is conceivable that Al is dissolved in the steel melt. For these cases we include the inter-metallic AlFe compound. The paramagnetic [12] AlFe crystallizes in the primitive cubic CsCl structure type. The compound is modeled here as a ferromagnet. We consider the error arising from the wrong type of magnetic order as lower than the error that is caused by disregarding the atomic magnetic moments altogether.

The ground state of iron is a bcc ferromagnet. The high-temperature phase present below the melting point is also bcc, but paramagnetic. Thus the ground-state structure should be a reasonable model in our case.

3. DFT calculations

All our DFT calculations are based on the linear augmented plane wave (LAPW) method as implemented in the WIEN2K

package [13]. The basis set consists of spherical harmonics within non-overlapping muffin-tin spheres around the atoms augmented by spacially unrestricted plane waves in the space outside the muffin-tin spheres. The core electrons are treated separately in atomic basis functions. The kinetic energy cut-off for the plane-wave basis functions is adjusted by the product of the smallest muffin-tin radius times the largest plane wave vector ($R_{MT}k_{max}=8$). The MT radii in the calculations presented here vary between 1.72–1.85 (Fe), 1.56–1.70 (Al) and 1.53–1.65 (O) in $a_0=0.52917$ Å.

The PBE-GGA [14] exchange correlation functional was applied in all calculations, which requires a good resolution of the total potential. This was ensured by increasing the maximum $\rightarrow g^{\rightarrow}$ vector for the series expansion of the total potential to a value of 20 Ry. In Fe containing phases, the magnetism was accounted for using a spin-dependent electron density in a scalar relativistic approximation. For some of the antiferromagnetic calculations, the symmetry had to be lowered to introduce independent sites. Table 1 lists various information for the calculations. For larger unit cells, comprising many atoms, less $\rightarrow k^{\rightarrow}-$points are needed, and in general, metals need a better Brillouin zone sampling than insulators.

The total energy minimum as a function of volume was searched by varying the crystal volume and computing the corresponding total energies. For these calculations, the space group symmetry was fixed, but other unit cell parameters were refined whenever this was computationally feasible. The relaxation was considered complete when all interatomic force components were smaller than 3 mRy/a_0. Only for the large unit cell of $\gamma-Al_2O_3$, this had to be lifted to 6 mRy/a_0. For the $\alpha-Al_2O_3$ structure, a full relaxation including the *c/a* ratio and atomic site parameters was done for each volume. However, the *c/a* ratio is found constant for all volume points of $\alpha-Al_2O_3$ considered. For structures containing more free sites, the unit cell geometry was only relaxed at a point near the equilibrium volume V_0, but the atomic sites were refined for each volume. In the low-symmetry $\gamma-Al_2O_3$, only 16 atomic sites were relaxed and only for V_0. In this case, the low symmetry results from the Al vacancies in the spinel lattice. The geometry was not changed to keep the underlying cubic spinel lattice. For the same reason, the c/a ratio of FeO was not touched. The systematic energy deviation resulting from non-relaxed structures can be estimated from our calculations at maximum of 10% of the total energy difference due to volume change.

Table 1
Summary of computational details: symmetry and centering for calculation (including magnetism); N_{At},ind.: symmetry-independent atoms per primitive unit cell; N_{At},full: all atoms per unit cell including centering; N_k,irr.: k-points in irreducible part of the BZ; N_k,full: k-points per complete BZ; metal/bandgap; spin ordering: FM parallel, AFM antiparallel.

Compound	Symmetry	N_{At} (ind./full)	N_k (irr./full)	m/g	Spins
Fe bcc	bcc	1/2	3654/148 877	m	FM
FeAl	Cubic P	2/2	816/29 791	m	FM
$FeAl_2O_4$	fcc	3/56	256/8000	m	FM
$AlFe_2O_4$	Tetragonal P	5/28	140/1960	m	AFM
$FeAlO_3$	Orthorhombic P	10/40	72/504	g	AFM
FeO	Tetragonal P	4/4	624/8464	m	AFM
α-Al_2O_3	Rhombohedral	2/30	770/8000	g	–
$\kappa-Al_2O_3$	Orthorhombic P	10/40	72/504	g	–
$\gamma-Al_2O_3$	Monoclinic C	16/80	210/784	g	–

The calculated energy–volume data, 15 points for each case, were fitted to a Birch–Murnaghan equation of state for solids [15]

$$E(V)=E_0+\frac{9V_0B_0}{16}\left[\left(\frac{V_0}{V}\right)^{2/3}-1\right]^3 B'_0+\left[\left(\frac{V_0}{V}\right)^{2/3}-1\right]^2\left[6-4\left(\frac{V_0}{V}\right)^{2/3}\right] \quad (1)$$

The total energy is determined by the self-consistent cycle, and must be sufficiently converged to get a well-defined energy difference between two volume points. For large unit cells as $\kappa-Al_2O_4$, a value of 10^{-4} eV is a suitable convergence limit, while for bcc Fe a value of 10^{-6} eV is required. The standard deviation of the fit to the EOS then ranges from 10^{-5} eV (bcc Fe) to 10^{-3} eV for Fe_2AlO_4. The latter could be in principle improved by lowering the force convergence requirement for the relaxation.

The Birch–Murnaghan equation thus describes the calculated volume-energy dependence fairly well. An example is shown in Fig. 2. The four parameters of the equation are determined by the fit: the isotropic bulk modulus (isothermal compressibility) B, its pressure derivative $\partial B/\partial p$ and the equilibrium volume V_0 and total energy E_0 at equilibrium volume. The minimum total energy E_0 represents the thermodynamic free enthalpy $F(V,T=0)$ at 0 K. The pressure-dependent Gibbs enthalpy $G(p,T=0)$ can be calculated using standard thermodynamic relations

$$G=E+pV \quad (2)$$

$$p=-\partial E/\partial V \quad (3)$$

using the Birch–Murnaghan energy (1) as an inner energy. The calculated pressure values for our *E–V* curves are mostly in the range $\pm$ 10 GPa, the maximum is 12 GPa.

Due to the application of periodic boundary conditions and fixed nuclei in the most common DFT methods, they are not

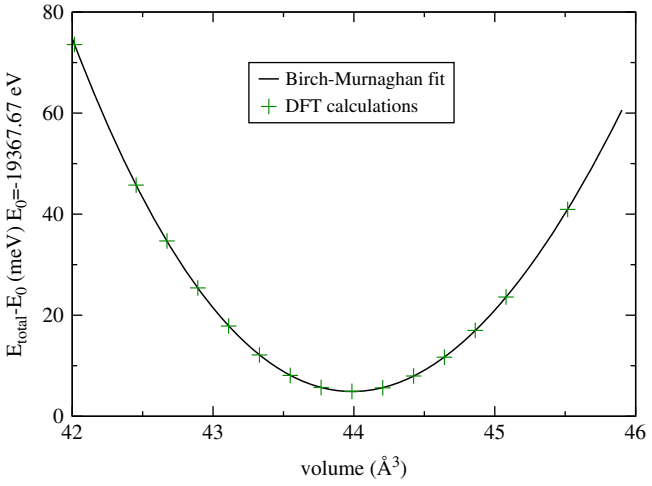

Fig. 2. Energy–volume curve for corundum. The values correspond to one formula unit of Al_2O_3. The line is calculated from the Birch–Murnaghan equation fitted to the calculated DFT data.

suited for properly modeling a liquid phase. However, of all compounds discussed here, only Al_2O_3 and $FeAl_2O_4/AlFe_2O_4$ are solid at temperatures higher than the melting temperature of iron. As an estimate for the energy difference between solid and liquid, we consider the value of the latent heat of fusion. The heat of fusion differs considerably between metals and their oxides (Fe: 0.14 eV/atom, Al: 0.11 eV/atom, FeO: 0.25 eV/f.u., Al_2O_3: 1.15 eV/f.u. [16]). From these values we construct $c_{FeAl} \approx c_{Fe} + c_{Al} = 0.25$ eV/f.u., $c_{FeAlO3} \approx c_{FeO} + 1/2 c_{Al2O3} = 0.825$ eV/f.u. as approximation for the remaining liquid phases. The total energy of a solid is increased by the heat of fusion when it melts.

4. Results and discussion

As described in the previous section we calculated the energy–volume dependence for all systems mentioned in Section 2. The data obtained from the fit to the Birch–Murnaghan equation of states are displayed in Table 2. Comparing these values to other theoretical data is difficult, because the result depends strongly on the level of theory applied. DFT calculations for Al_2O_3 [17,18] show the dependence on the type of exchange-correlation potential. We list a comparison of some selected theoretical and experimental data in Table 3. This is to show that our results are comparable to other DFT calculations, and their deviations from measurements are also typical for the method applied. For the iron-containing oxides and even FeAl, the appropriate DFT method would be DFT+U, which introduces an orbital-dependent potential to describe the localized *d* electrons. However, the elastic properties are for example in FeO already well described by GGA [19], while GGA+U is needed for a good electronic structure calculation. In view of this, we decided not to use DFT+U.

4.1. Alumina phases

The calculated properties of the alumina phases are collected in Table 2. There is a notable difference in the volume per formula unit, V_0. The stable corundum has the lowest volume. Experiments show that $\kappa-Al_2O_3$ coatings produced by CVD develop cracks during the transformation to the $\alpha-$phase [20].

Table 2
Calculated data: V_0 is the equilibrium volume at zero pressure per formula unit, B is the bulk modulus.

Compound	Structure	B (GPa)	V_0/f.u. (Å^3)	$\partial B/\partial p$
$\alpha-Al_2O_3$	Corundum	230	44.0	4.2
$\gamma-Al_2O_3$	Defect-spinel	210	47.6	4.1
$\kappa-Al_2O_3$	$FeAlO_3$	199	46.5	4.0
$FeAlO_3$	$FeAlO_3$	170	50.5	4.1
$FeAl_2O_4$	Spinel	189	69.6	4.1
Fe_2AlO_4	Inverse-spinel	170	71.4	4.2
FeO	NaCl	172	20.2	4.2
Fe	bcc	199	11.3	5.4
FeAl	CsCl	175	23.7	4.1

This behavior appears to be consistent with our calculated volume data. The differences in volume and bulk modulus agree with the findings of other authors [18].

The total energy differences of the Al_2O_3 phases compared to corundum are small: 0.08 eV for $\kappa-Al_2O_3$ and 0.22 eV for $\gamma-Al_2O_3$ at zero pressure. Thus the enthalpy–pressure curves of all phases shown in Fig. 3 are very close together. The increase in total energy is accompanied by an increase in V_0 in the same sequence.

The calculated phase transformations from the most stable $\alpha-$phase to $\gamma-$ or $\kappa-Al_2O_3$ would occur at negative pressure, i.e. in case of an expansion of the lattice (see in Fig. 3). This condition may be achieved for instance through chemical pressure by impurity atoms or strain in case of epitaxial growth.

4.2. Phase formation in the presence of iron

The experimental observations indicate the formation of new crystal phases on the filter surface. Using the calculated total energies, the enthalpy differences between several possible phases can be calculated. This difference is determined by the energy gain from chemical bonding only, because thermal

Table 3
Theoretical and experimental data from the literature.

Compound	DFT			Experiment	
	B (GPa)	V_0/f.u. (Å^3)		B (GPa)	V_0/f.u. (Å^3)
$\alpha-Al_2O_3$	241	41.0 [22]	GGA	258	42.5 [23]
$\kappa-Al_2O_3$	224	45.2 [18]	GGA		49.3 [10]
$\gamma-Al_2O_3$	219	46.0 [6]	LDA	162	46.3 [24]
$FeAl_2O_4$	185	67.9 [25]	GGA	191	66.0 [26]
FeO	169	19.7 [19]	GGA	154	19.9 [27]
Fe bcc	185	11.6 [28]	GGA	166	11.8 [29]
FeAl	181	23.9 [30]	GGA	138	24.6 [31]

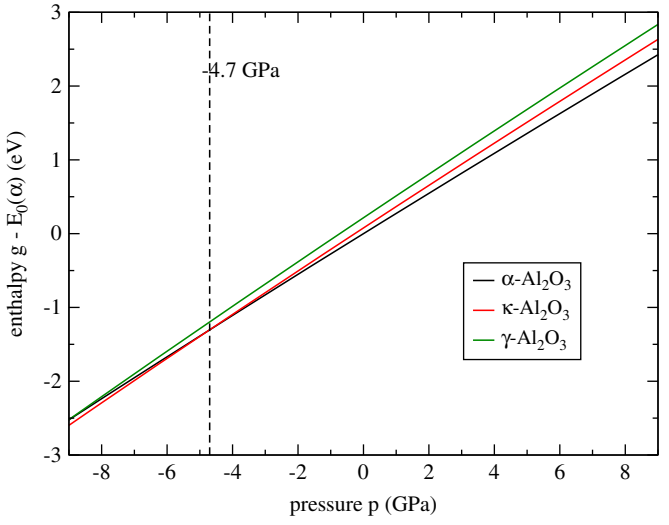

Fig. 3. Enthalpy as a function of pressure $g(p,T=0)$ for $\alpha-$, $\gamma-$ and $\kappa-$alumina.

Table 4
Energy differences ΔE for Reactions $A \leftrightarrow B$ calculated as $\Delta E = E_B - E_A$ using the equilibrium zero pressure total energy from DFT calculations. Negative values indicate preference of the B side. In ΔE_c, the heat of fusion is included for the presumably liquid phases (Fe, FeAl, FeO, $FeAlO_3$). $\Delta V = V_B - V_A$ is the volume difference of the ground state phases.

#	Reaction	ΔE (eV)	ΔE_c (eV)	ΔV(Å^3)
1.	Al_2O_3 + 2 Fe ↔ $FeAlO_3$ + FeAl	3.6	4.6	8.8
2.	Al_2O_3 + 5/4 Fe ↔ 3/4 $FeAl_2O_4$ + 1/2 FeAl	2.1	2.0	6.6
3.	Al_2O_3 + 11/4 Fe ↔ 3/4 Fe_2AlO_4 + 5/4 FeAl	4.3	4.3	9.7
4.	Al_2O_3 + 3 FeO ↔ 2 $FeAlO_3$ + Fe	−1.8	−0.2	7.1
5.	Al_2O_3 + FeO ↔ $FeAl_2O_4$	−0.2	−0.5	5.4
6.	Al_2O_3 + FeO + 2 Fe ↔ Fe_2AlO_4 + FeAl	2.8	2.5	8.5
7.	Al_2O_3 + 5 FeO ↔ Fe_2AlO_4 + Fe	−3.2	−4.4	9.5
8.	Al_2O_3 + 5 Fe ↔ 3 FeO + 2 FeAl	8.9	9.4	7.6

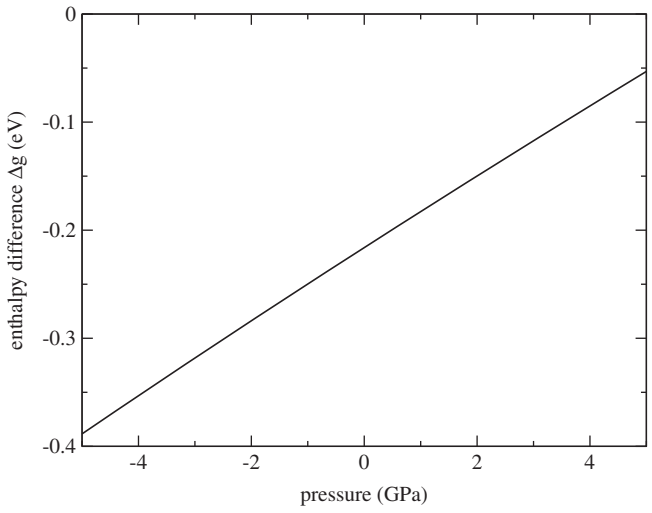

Fig. 4. Enthalpy $g(p,T=0)$ for the reaction $Al_2O_3 + FeO \leftrightarrow FeAl_2O_4$. Calculated without heat of fusion (see Table 4).

effects are not included here. We consider reactions shown in Table 4 of Al_2O_3 with Fe (rows 1–3), and with FeO (rows 4–7). The energies are calculated per formula unit of Al_2O_3 to make them comparable. Only the reactions of Al_2O_3 with FeO result in an energy gain, producing hercynite or $FeAlO_3$. Fe_2AlO_4 is unstable when the concentration of FeO is low (reaction no. 6) and becomes stable at high FeO concentrations (reaction no. 7). The stabilization of $FeAlO_3$ (reaction no. 4) similarly occurs at high FeO concentration. In general, higher concentrations of FeO on the left side result in higher values of the energy gain. The reason for the energy gain here seems to be the instability of FeO. Its formation is directly compared to that of Al_2O_3 in reaction no. 8.

In the column ΔE_c of Table 4, the heat of fusion as discussed in Section 3 is added to the negative total energy for all liquid phases. The idea is to have a rough estimate for the influence of the elevated temperature, near the melting point of iron. This changes the energy differences for the reactions, but the assessment of likely and unlikely reactions does not change. Besides, when comparing the values for reaction no. 5 to the experimental result for the free energy of formation at high temperature reported in [21] (−3490 cal./mol ≈0.15 eV/f.u.), the energy without heat of fusion is in better agreement.

Replacing corundum by the metastable alumina phases adds the additional energy difference with respect to the α−phase discussed before and decreases the reaction energies. Therefore, if metastable phases are present on the filter surfaces, they will be the preferred reaction sites. However, the overall change in energy is too small to open completely new reaction pathways.

Table 4 also contains information about the change in volume for each of the reactions at zero pressure. The positive values indicate that all reactions cause an expansion. As can be seen from the pressure dependence of the hercynite formation reaction shown in Fig. 4, the enthalpy approaches zero with increasing pressure, thereby destabilizing hercynite.

5. Conclusion

Our results show that the formation of the hercynite ($FeAl_2O_4$) phase beginning from alumina (Al_2O_3) and Fe is not directly possible in thermodynamic equilibrium. An incorporation of dissolved Al_2O_3 in hercynite would be equivalent to the unfavorable reaction no. 2 of Table 4. The experimental reports, finding hercynite at the interface of alumina filters and steel melts desire another explanation. We could show that adding of oxygen in the form of FeO enables a reaction with Al_2O_3. We expect a similar behavior for a low concentration of oxygen dissolved in Fe (FeO_δ). Here we have to ask ourselves, how the extra oxygen is provided in the experimental process. The simplest possibility is an oxygen enrichment of the melt from the air or from the melting process. It is clear that the formation of compounds with Fe^{2+} like FeO or hercynite occurs in a regime of low oxygen concentration only. Higher oxygen concentrations could stabilize higher oxidized iron ions, like Fe^{3+} in Fe_2AlO_4. But these reaction products would have to compete with iron oxides like Fe_2O_3.

Another option discussed by Paesano et al. [4] is the formation of hercynite containing oxygen vacancies as a primary step. Such a process could be caused by diffusion of iron into rhombohedral corundum (as for example in sapphire). This appears also likely because the alumina and Fe–alumina

phases share several common crystal structures. On the other hand, the energy gain for vacancy-containing hercynite should be even less favorable than the value for the formation reaction (5).

For the filter process discussed, a certain degree of phase formation may be important to act as 'glue' between the filter surface and adhering particles. Also the binding of oxygen in chemical reactions is a desirable process.

Acknowledgments

This work was supported by the DFG in the framework of the Collaborative Research Center 920: 'Multi-Functional Filters for Metal Melt Filtration–A Contribution towards Zero Defect Materials'. The authors are grateful for the numerous fruitful and informative discussions and suggestions within that project. We thank the Center for Information Services and High Performance Computing ZIH Dresden for the computational support.

References

[1] K. Wasai, K. Mukai, A. Miyanaga, Observation of inclusion in aluminum deoxidized iron, ISIJ International 42 (2002) 459–466.
[2] C.G. Aneziris, S. Dudczig, J. Hubálková, M. Emmel, G. Schmidt, Alumina coatings on carbon bonded alumina nozzles for active filtration of steel melts, Ceramics International 39 (3) (2013) 2835–2843.
[3] R.B. Tuttle, J.D. Smith, K.D. Peaslee, Casting simulation of calcium titanate and calcium zirconate nozzles for continuous casting of aluminium-killed steels, Metallurgical and Materials Transactions B 38 (2007) 101–108.
[4] A. Paesano Jr., C. Matsuda, J. da Cunha, M. Vasconcellos, B. Hallouche, S. Silva, Synthesis and characterization of Fe–Al_2O_3 composites, Journal of Magnetism and Magnetic Materials 264 (2–3) (2003) 264–274.
[5] B. Ollivier, R. Retoux, P. Lacorre, D. Massiot, G. Ferey, Crystal structure of κ−alumina: an X-ray powder diffraction TEM, and NMR study, Journal of Materials Chemistry (1997) 1049–1056.
[6] G. Gutiérrez, A. Taga, B. Johansson, Theoretical structure determination of γ−Al_2O_3, Physical Review B 65 (2001) 012101.
[7] H. Fjellvåg, F. Grønvold, S. Stølen, B. Hauback, On the crystallographic and magnetic structures of nearly stoichiometric iron monoxide, Journal of Solid State Chemistry 124 (1996) 52–57.
[8] R.J. Hill, X-ray powder diffraction profile refinement of synthetic hercynite, American Mineralogist 69 (1984) 937–942.
[9] A. Walsh, S.-H. Wei, Y. Yan, M.M. Al-Jassim, J.A. Turner, M. Woodhouse, B.A. Parkinson, Structural, magnetic, and electronic properties of the Co–Fe–Al oxide spinel system: density-functional theory calculations, Physical Review B 76 (2007) 165119.
[10] F. Bouree, J.L. Baudour, E. Elbadraoui, J. Musso, C. Laurent, A. Rousset, Crystal and magnetic structure of piezoelectric, ferrimagnetic and magnetoelectric aluminium iron oxide $FeAlO_3$ from neutron powder diffraction, Acta Crystallographica Section B 52 (1996) 217–222.
[11] P. Kumar, A. Bera, D.V.S. Muthu, S.N. Shirodkar, R. Saha, A. Shireen, A. Sundaresan, U.V. Waghmare, A.K. Sood, C.N.R. Rao, Coupled phonons, magnetic excitations, and ferroelectricity in $AlFeO_3$: Raman and first-principles studies, Physical Review B 85 (2012) 134449.
[12] S.A. Makhlouf, T. Nakamura, M. Shiga, Structure and magnetic properties of $FeAl_{1x}Rh_x$ alloys, Journal of Magnetism and Magnetic Materials 135 (1994) 257–264.
[13] P. Blaha, K. Schwarz, G.K.H. Madsen, D. Kvasnicka, J. Luitz, WIEN2k, An Augmented Plane Wave+Local Orbitals Program for Calculating Crystal Properties, Technische Universität Wien, Austria, version 11.1, 2001.
[14] J.P. Perdew, K. Burke, M. Ernzerhof, Generalized gradient approximation made simple, Physical Review Letters 77 (1996) 3865–3868.
[15] F. Birch, Finite elastic strain of cubic crystals, Physical Review 71 (1947) 809–824.
[16] D.R. Lide (Ed.), CRC Handbook of Chemistry and Physics, CRC Press, 2003.
[17] J.C. Boettger, High-precision, all-electron, full-potential calculation of the equation of state and elastic constants of corundum, Physical Review B 55 (1997) 750–756.
[18] S.J. Mousavi, M.R. Abolhassani, S.M. Hosseini, S.A. Sebt, Comparison of electronic and optical properties of the α and κ phases of alumina using density functional theory, Chinese Journal of Physics 47 (2009) 862–873.
[19] W.-B. Zhang, Y.-H. Deng, Y.-L. Hu, K.-L. Han, B.-Y. Tang, Structural distortion of $B1$-structured MnO and FeO, Solid State Communications 142 (1–2) (2007) 6–9.
[20] N. Lindulf, M. Halvarsson, H. Nordén, S. Vuorinen, Microstructural investigation of the κ−$Al_2O_3 \rightarrow \alpha$−$Al_2O_3$ transformation in multilayer coatings of chemically vapour deposited κ−Al_2O_3, Thin Solid Films 253 (1994) 311–317.
[21] T.C.M. Pillay, J. D'Entremont, J. Chipman, Stability of hercynite at high temperatures, Journal of the American Ceramic Society 43 (11) (1960) 583–585.
[22] M. Iuga, G. Steinle-Neumann, J. Meinhardt, Ab-initio simulation of elastic constants for some ceramic materials, European Physical Journal B 58 (2) (2007) 127–133.
[23] L.S. Dubrovinsky, S.K. Saxena, P. Lazor, High-pressure and high-temperature in situ X-ray diffraction study of iron and corundum to 68 GPa using an internally heated diamond anvil cell, Physics and Chemistry of Minerals 25 (1998) 434–441.
[24] M.R. Gallas, G.J. Piermarini, Bulk modulus and Young's modulus of nanocrystalline-alumina, Journal of the American Ceramic Society 77 (11) (1994) 2917–2920.
[25] S. Ono, J. Brodholt, G. Price, First-principles simulation of high-pressure polymorphs in $MgAl_2O_4$, Physics and Chemistry of Minerals 35 (2008) 381–386.
[26] D. Levy, A. Pavese, M. Hanfland, Synthetic $MgAl_2O_4$ (spinel) at high-pressure conditions (0.0001–30 GPa): a synchrotron X-ray powder diffraction study, American Mineralogist 88 (1) (2003) 93–98.
[27] M. Liu, L. Liu, Bulk moduli of wüstite and periclase: a comparative study, Physics of the Earth and Planetary Interiors 45 (3) (1987) 273–279.
[28] M. Ekman, B. Sadigh, K. Einarsdotter, P. Blaha, Ab initio study of the martensitic bcc–hcp transformation in iron, Physical Review B 58 (1998) 5296–5304.
[29] H.M. Ledbetter, R.P. Reed, Elastic properties of metals and alloys, I. Iron, nickel, and iron–nickel alloys, Journal of Physical and Chemical Reference Data 2 (3) (1973) 531–618.
[30] P. Novák, J. Kuneš, L. Chaput, W.E. Pickett, Exact exchange for correlated electrons, Physica Status Solidi (B) 243 (3) (2006) 563–572.
[31] R.L. Clendenen, H.G. Drickamer, Effect of high pressure on the compressibilities of five alloys, Journal of Chemical Physics 44 (12) (1966) 4385–4386.